Star formation near the Sun is driven by expansion of the Local Bubble

https://doi.org/10.1038/s41586-021-04286-5

Received: 18 August 2021

Accepted: 26 November 2021

Published online: 12 January 2022

Check for updates

Catherine Zucker[1,2]✉, Alyssa A. Goodman[1], João Alves[3], Shmuel Bialy[1,4], Michael Foley[1], Joshua S. Speagle[5,6,7], Josefa Großschedl[3], Douglas P. Finkbeiner[1,8], Andreas Burkert[9,10], Diana Khimey[1] & Cameren Swiggum[3,11]

For decades we have known that the Sun lies within the Local Bubble, a cavity of low-density, high-temperature plasma surrounded by a shell of cold, neutral gas and dust[1–3]. However, the precise shape and extent of this shell[4,5], the impetus and timescale for its formation[6,7], and its relationship to nearby star formation[8] have remained uncertain, largely due to low-resolution models of the local interstellar medium. Here we report an analysis of the three-dimensional positions, shapes and motions of dense gas and young stars within 200 pc of the Sun, using new spatial[9–11] and dynamical constraints[12]. We find that nearly all of the star-forming complexes in the solar vicinity lie on the surface of the Local Bubble and that their young stars show outward expansion mainly perpendicular to the bubble's surface. Tracebacks of these young stars' motions support a picture in which the origin of the Local Bubble was a burst of stellar birth and then death (supernovae) taking place near the bubble's centre beginning approximately 14 Myr ago. The expansion of the Local Bubble created by the supernovae swept up the ambient interstellar medium into an extended shell that has now fragmented and collapsed into the most prominent nearby molecular clouds, in turn providing robust observational support for the theory of supernova-driven star formation.

In Fig. 1a (Supplementary Fig. 1), we present a three-dimensional (3D) map of the solar neighbourhood, including a new Gaia-era 3D model of the Local Bubble's inner surface of neutral gas and dust[10,13] and the 3D shapes and positions of local molecular clouds constrained at approximately 1 pc resolution[9,11]. The Local Bubble's shell is shown as a closed surface, but evidence suggests it could be a 'Galactic chimney', having blown out of the disk a few hundred parsecs above and below the Galactic plane[14]. The distribution of dense gas in star-forming molecular clouds is shown with a set of topological 'spines' derived by 'skeletonizing' the clouds in 3D volume density space[11].

We find that every well-known molecular cloud within approximately 200 pc of the Sun lies on the surface of the Local Bubble. These 'surface' clouds include not just every star-forming region in the Scorpius-Centaurus (Sco-Cen) association (Ophiuchus, Lupus, Pipe, Chamaeleon and Musca), but also the Corona Australis region and the Taurus Molecular Cloud, the latter of which lies 300 pc away from Sco-Cen on the opposite side of the bubble. The one exception is the Perseus Molecular Cloud, at a distance of 300 pc, which has probably been displaced by the recently discovered Per-Tau Superbubble[15], containing Taurus on its near side and Perseus on its far side (see the green sphere in Fig. 1b (Supplementary Fig. 1)). The Taurus Molecular Cloud complex lies at the intersection of the Per-Tau Bubble and Local Bubble, displaying a sheet-like morphology consistent with being shaped by a bubble–bubble collision. Every Local Bubble surface cloud shows evidence of a similar sheet-like (for example, Taurus) or filamentary (for example, Corona Australis) morphology, uniformly elongated along the bubble's surface.

In Fig. 1b, in addition to the Local Bubble surface, we show models for two kiloparsec-scale Galactic features discovered in the *Gaia* era: the Radcliffe Wave[16] and the Split[10]. The Radcliffe Wave is a 2.7-kpc-long filament of gas corresponding to the densest part of the Local Arm of the Milky Way. It has the shape of a damped sinusoid, extending above and below the plane of the Galaxy[16]. The Split, an at least 1-kpc-long gaseous feature situated in the disk, is argued to be a spur-like feature, bridging the Local and Sagittarius-Carina arms[10]. Also shown (in the interactive version in Supplementary Fig. 1 only) is a model of the Gould's Belt, a disk of young stars, gas and dust, tilted by about 20° with respect to the Galactic plane, which has long shaped our understanding of the architecture of the local interstellar medium. Previous work has suggested that the Gould's 'Belt' is a superposition of unassociated structures seen in projection, with all well-known regions of the 'Belt' being part of either the Radcliffe Wave or the Split large-scale gaseous structures[16]. As illustrated in Fig. 1b (and the interactive version in Supplementary Fig. 1), this argument about the nature of the Gould's Belt is confirmed here. The right-hand side of the assumed Gould's Belt (the Sco-Cen association) consists of the entire rightward wall of the Local

[1]Center for Astrophysics | Harvard & Smithsonian, Cambridge, MA, USA. [2]Space Telescope Science Institute, Baltimore, MD, USA. [3]Department of Astrophysics, University of Vienna, Wien, Austria. [4]Department of Astronomy, University of Maryland, College Park, MD, USA. [5]Department of Statistical Sciences, University of Toronto, Toronto, Ontario, Canada. [6]David A. Dunlap Department of Astronomy & Astrophysics, University of Toronto, Toronto, Ontario, Canada. [7]Dunlap Institute for Astronomy & Astrophysics, University of Toronto, Toronto, Ontario, Canada. [8]Harvard University Department of Physics, Cambridge, MA, USA. [9]University Observatory Munich, Munich, Germany. [10]Max-Planck-Institut für extraterrestrische Physik, Garching, Germany. [11]Department of Astronomy, University of Wisconsin, Madison, WI, USA. ✉e-mail: catherine.zucker@cfa.harvard.edu

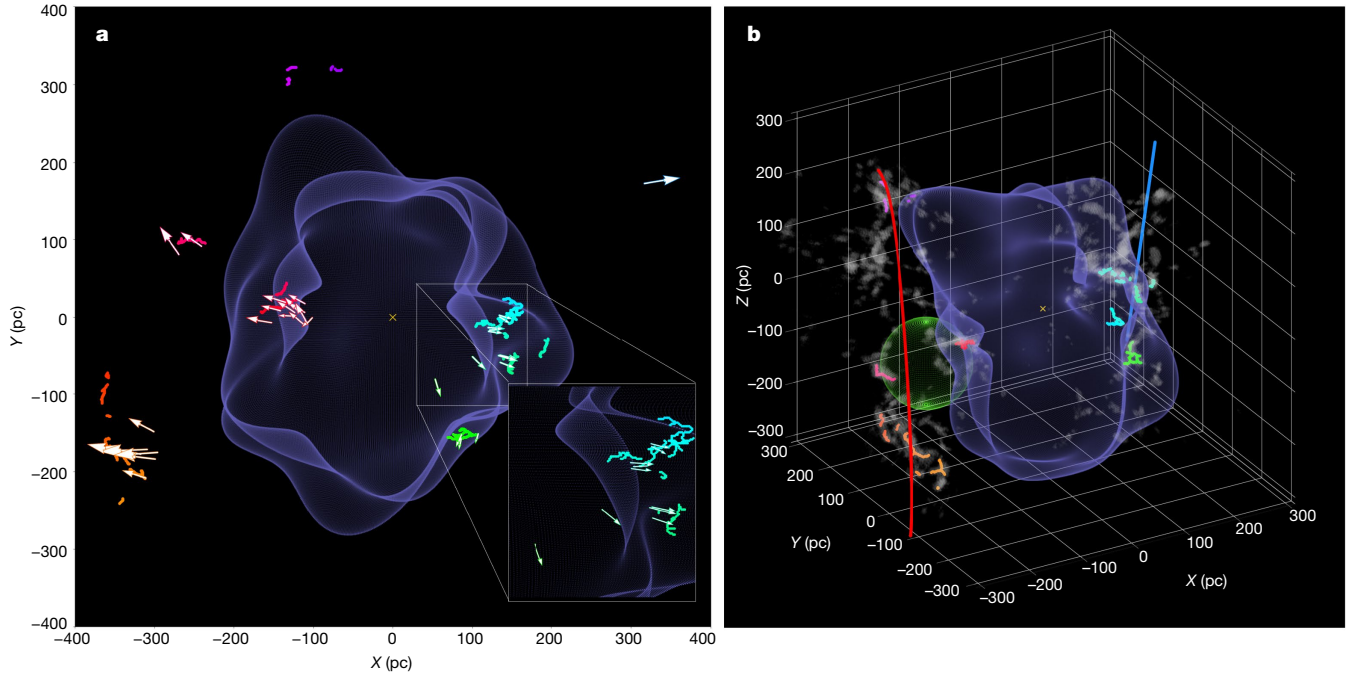

Fig. 1 | A 3D spatial view of the solar neighbourhood. For the best experience, please view the online 3D interactive version available in Supplementary Fig. 1. **a**, A top-down projection of star-forming regions on the surface of the Local Bubble, whose young stars show motion mainly perpendicular to its surface. The surface of the Local Bubble[13] is shown in purple. The short squiggly coloured lines (or 'skeletons') demarcate the 3D spatial morphology of dense gas in prominent nearby molecular clouds[11]. The 3D arrows indicate the positions of young stellar clusters, with the apex of the arrow's cone pointing in the direction of stellar motion. Clusters are colour-coded by longitude, as in Extended Data Table 1. The Sun is marked with a yellow cross. The enlargement to the lower right shows a close-up of Ophiuchus, Pipe, Lupus and Corona Australis on the bubble's surface, along with arrows illustrating the outward motion of their young stellar clusters. **b**, A 3D view of the relationship between the Local Bubble, prominent nearby star-forming regions and Galactic structure. The Local Bubble and cloud skeletons are the same as in **a**. We also overlay the morphology of the 3D dust (grey blobby shapes[9]) and the models for two Galactic scale features—the Radcliffe Wave (red)[16] and the Split (blue)[10]. The Per-Tau Superbubble[15] (green sphere) is also overlaid. The interactive version offers views from any direction (not just top-down), provides floating labels for star-forming regions and includes additional layers (some not shown in this snapshot), which can be toggled on/off.

Bubble, whereas its left-hand side consists of clouds in the Radcliffe Wave, well beyond the leftward wall of the Local Bubble. The Local Bubble lies at the closest distance between the Radcliffe Wave and the Split, with most of the dense gas at its surface co-spatial with these two kiloparsec-scale features.

We use measurements of the 3D positions and motions of stellar clusters to reconstruct the star formation history near the Local Bubble. We rely on curated samples of young stars from the literature, as summarized in Extended Data Table 1. Our sample includes: clusters associated with star-forming regions on the surface of the bubble (Taurus, Ophiuchus, Lupus, Chamaeleon and Corona Australis), older members of the Sco-Cen association (Upper Centaurus Lupus (UCL), Lower Centaurus Crux (LCC) and Upper Scorpius) up to a maximum age of 20 Myr; and clusters in known star-forming regions along the Radcliffe Wave and the Split but beyond the boundaries of the Local Bubble itself (Perseus, Serpens and Orion).

As described in the Methods, we derive the 'tracebacks' of stellar clusters associated with the Local Bubble and related structures. The current 3D space motions of the young stellar clusters are shown as cones in Supplementary Fig. 1 with the apex of the cone pointing in the direction of motion. Previous research has shown that the 3D space motions of the youngest clusters ($\lesssim$3 Myr) can be considered probes of the 3D space motions of the parental gas clouds in which they were born[17]. Using the young stars' motions to trace cloud motion, we see that not only do all star-forming clouds presently observed within 200 pc lie on the surface of the Local Bubble, but they also show strong evidence of outward expansion, primarily perpendicular to the bubble's surface. Tracebacks of the clusters' motions over the past 20 Myr point to the likely origin of the Local Bubble—presumably the region where the supernovae driving the bubble went off. The clear implication of the observed geometry and motions is that all of the well-known star-forming regions within 200 pc of the Sun formed as gas was swept up by the Local Bubble's expansion.

Supplementary Fig. 1 also includes a model for Gould's Belt[18], which illustrates that much of the motion previously attributed to the expansion of the assumed Gould's Belt[19] is instead probably due to the expansion of the Local Bubble. Recent work using complementary catalogues of young stars bolster this interpretation, finding evidence that the Sco-Cen stellar association—a key anchor of the Gould Belt—has an arc-like morphology consistent with recent sequential star formation, which we now know to be triggered by the Local Bubble[20].

A full animation of the stellar tracebacks is provided in Fig. 2 (Supplementary Fig. 2). In the static version, we show select snapshots at −16 Myr, −15 Myr, −14 Myr, −10 Myr, −6 Myr, −2 Myr and the present day. We observe multiple epochs of star formation, with each generation of stars consistent with being formed at the edge of the Local Bubble's expanding shell. We find that 15–16 Myr ago, the UCL and LCC clusters in the Sco-Cen stellar association were born about 15 pc apart, and that the Bubble itself was probably created by supernovae whose surviving members belong to these clusters.

On the basis of the amount of momentum injection required by supernovae to sweep up the total mass of the shell ($1.4^{+0.65}_{-0.62} \times 10^6\ M_\odot$) given its present-day expansion velocity ($6.7^{+0.5}_{-0.4}$ km s^{-1}), we estimate that 15^{+11}_{-7} supernovae were required to form the Local Bubble (Methods). Through an analysis of their existing stellar membership and an

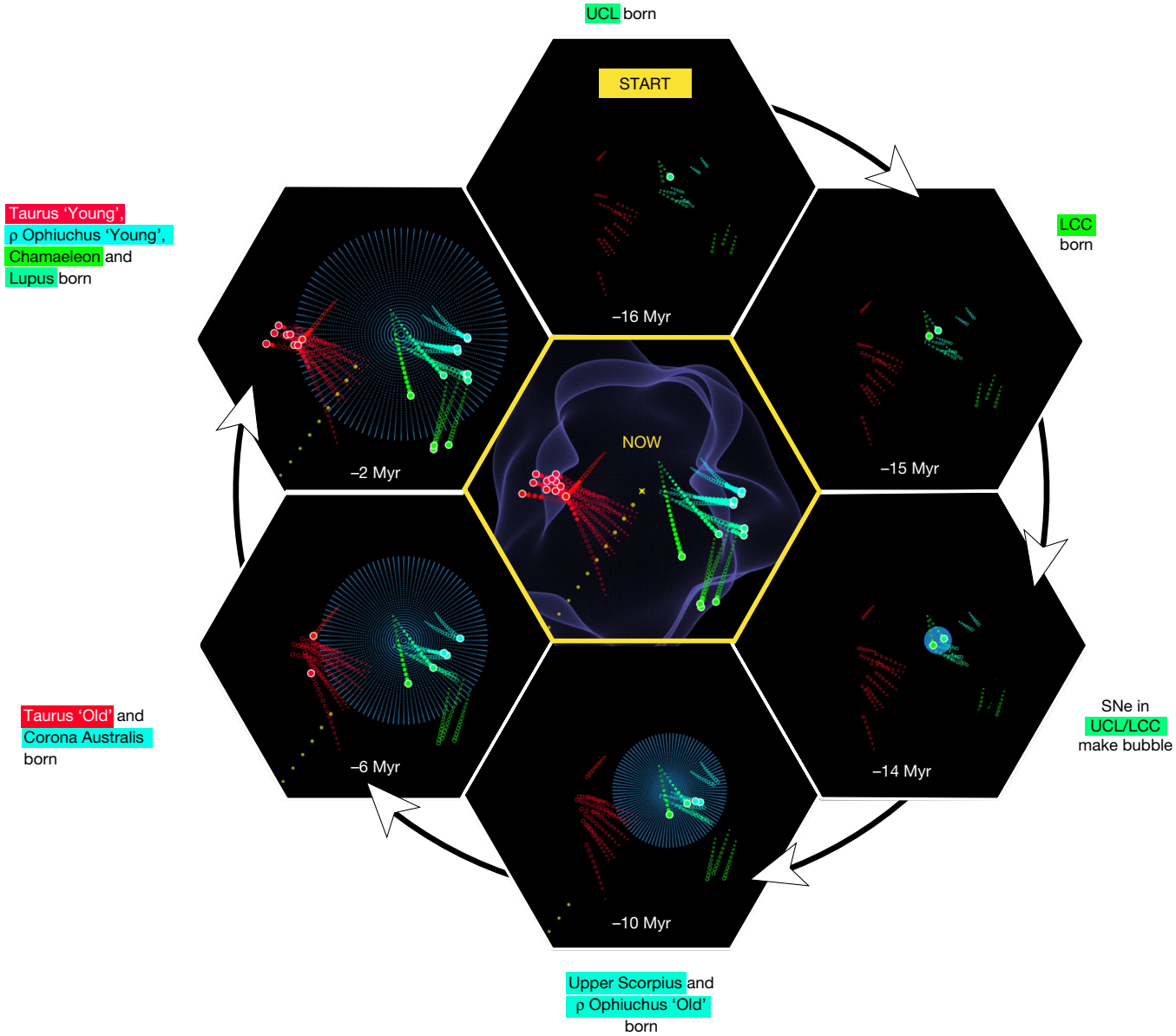

Fig. 2 | The evolution of the Local Bubble and sequential star formation at the surface of its expanding shell. Selected time snapshots (seen from a top-down projection) are shown here. For a full time-sequence, viewable from any angle (not just top-down), see the online 3D interactive version in Supplementary Fig. 2. The central figure shows the present day. Stellar cluster tracebacks are shown with the coloured paths. Before the cluster birth, the tracebacks are shown as unfilled circles meant to guide the eye, since our modelling is insensitive to the dynamics of the gas before its conversion into stars. After the cluster birth, the tracebacks are shown with filled circles and terminate in a large dot, which marks the cluster's current position. For time snapshots ≤14 Myr ago, we overlay a model for the evolution of the Local Bubble (purple sphere), as derived in the Methods. The position of the local standard of rest (LSR) corresponds to the centre of each panel. A more detailed overview of this evolutionary sequence, including the birth positions of all clusters, is provided in Extended Data Table 2. The solar orbit is shown in yellow and indicates that the Sun entered the Local Bubble approximately 5 Myr ago.

adopted initial mass function, previous studies agree that UCL and LCC have produced 14–20 supernovae over their lifetimes[6,7,21]. However, previous work[6,7] also claims that UCL and LCC formed outside the present-day boundary of the Local Bubble, only entering its interior in the past few megayears, inconsistent with an argument that they are the progenitor population. By adopting new *Gaia* EDR3 estimates of the clusters' 3D velocities, better orbit integration and a more accurate value for the Sun's peculiar motion, we find that UCL and LCC indeed coincide with the centre of the bubble at its birth, lying just interior to its inner surface in the present day, thereby resolving this discrepancy. We explain the inconsistency between the stellar tracebacks for UCL and LCC proposed in this work and those from previous work in more detail in the Methods[6,7].

Under the assumption that each star-forming molecular cloud formed because of the shell's expansion—powered by UCL and LCC near its centre—we fit for the temporal and radial evolution of the Local Bubble by building on recent analytic frameworks[22]. As described in the Methods, our idealized, spherical shell expansion model fits for the age of the Local Bubble, the duration between supernova explosions powering its expansion, and the ambient density of the interstellar medium before the first explosion. We find that an age of $14.4^{+0.7}_{-0.8}$ Myr, a time between supernova explosions of $1.1^{+0.6}_{-0.4}$ Myr and an ambient density of $2.7^{+1.6}_{-1.0}$ cm^{-3} provides the best-fit to the dynamical tracebacks. This best-fit model for the Local Bubble's expansion is also shown in Fig. 2 (static version) and Supplementary Fig. 2 (interactive version).

After the presumed birth of the Local Bubble 14 Myr ago, we observe four subsequent epochs of star formation at the surface of its expanding shell, taking place approximately 10 Myr ago, 6 Myr ago, 2 Myr ago and the present day. Around 10 Myr ago, we observe the formation of the Upper Scorpius association, as well as an older, recently discovered companion stellar population in Ophiuchus. Next, 6 Myr ago, both Corona Australis and the older stellar population of Taurus were born. Around 2 Myr ago, we detect the birth of stars in Lupus and Chamaeleon, as well as the younger stellar populations of Taurus and Ophiuchus. Finally, in the present day, we observe the current distribution of dense star-forming molecular gas, enveloping the Local Bubble. In Fig. 2, we also overlay the solar orbit, which indicates that the Sun only entered the bubble around 5 Myr ago, and that it was about 300 pc away when the first supernovae went off in UCL and LCC. If this expanding shell scenario is true, we would expect a total of $1.7^{+0.97}_{-0.63} \times 10^6 M_\odot$ of gas to be swept up by the Local Bubble over its lifetime, given our inferred ambient density of $2.7^{+1.6}_{-1.0}$ cm^{-3} and the current radius of 165 ± 6 pc (Methods and Extended Data Fig. 2). On the basis of the 3D dust currently enveloping the shell's surface, we obtain an actual swept-up mass of $1.4^{+0.65}_{-0.62} \times 10^6 M_\odot$, in agreement with the model estimate.

The circumstances that led to the birth of the progenitor populations UCL and LCC are more difficult to constrain. Given the close proximity of both the Radcliffe Wave and the Split to the Local Bubble, the origin of UCL and LCC could be related to one of these kiloparsec-scale gaseous structures or to a past interaction between the two. Although current kinematic data are limited, the 3D tracebacks of young stars in two constituent clouds along the Radcliffe Wave (Orion) and the Split (Serpens), but beyond the Local Bubble's influence suggest that the Radcliffe Wave and the Split could have converged 20 Myr ago at the location where UCL and LCC were born. However, future follow-up work on the 3D motions of these two linear features would be needed to shed light on the true architecture of interstellar gas on kiloparsec scales at the time of the formation of UCL and LCC.

Regardless of the potential origins of UCL and LCC, we find six-dimensional (6D; 3D position and 3D velocity) observational support for the theory of supernova-driven star formation in the interstellar medium[23–26]—a long-invoked theoretical pathway for molecular cloud formation found in numerical simulations[27]. The abundance of new stellar radial velocity data expected in *Gaia* DR3 should not only enable more refined estimates of the Local Bubble's evolution, but also enable similar studies farther afield, providing further observational constraints on supernova-driven star formation across our Galactic neighbourhood.

Online content

Any methods, additional references, Nature Research reporting summaries, source data, extended data, supplementary information, acknowledgements, peer review information; details of author contributions and competing interests; and statements of data and code availability are available at https://doi.org/10.1038/s41586-021-04286-5.

1. Cox, D. P. & Reynolds, R. J. The local interstellar medium. *Annu. Rev. Astron. Astrophys.* **25**, 303–344 (1987).
2. Lucke, P. B. The distribution of color excesses and interstellar reddening material in the solar neighborhood. *Astron. Astrophys.* **64**, 367–377 (1978).
3. Sanders, W. T., Kraushaar, W. L., Nousek, J. A. & Fried, P. M. Soft diffuse X-rays in the southern galactic hemisphere. *Astrophys. J. Lett.* **217**, L87–L91 (1977).
4. Lallement, R., Welsh, B. Y., Vergely, J. L., Crifo, F. & Sfeir, D. 3D mapping of the dense interstellar gas around the Local Bubble. *Astron. Astrophys.* **411**, 447–464 (2003).
5. Welsh, B. Y., Lallement, R., Vergely, J.-L. & Raimond, S. New 3D gas density maps of NaI and CaII interstellar absorption within 300 pc. *Astron. Astrophys.* **510**, A54 (2010).
6. Fuchs, B., Breitschwerdt, D., de Avillez, M. A., Dettbarn, C. & Flynn, C. The search for the origin of the Local Bubble redivivus. *Mon. Not. R. Astron. Soc.* **373**, 993–1003 (2006).
7. Breitschwerdt, D. et al. The locations of recent supernovae near the Sun from modelling ^{60}Fe transport. *Nature.* **532**, 73–76 (2016).
8. Frisch, P. & Dwarkadas, V. V. in *Handbook of Supernovae* (eds Alsabti, A. W. & Murdin, P.) 2253–2285 (Springer International Publishing, 2017).
9. Leike, R. H., Glatzle, M. & Enßlin, T. A. Resolving nearby dust clouds. *Astron. Astrophys.* **639**, A138 (2020).
10. Lallement, R. et al. Gaia-2MASS 3D maps of Galactic interstellar dust within 3 kpc. *Astron. Astrophys.* **625**, A135 (2019).
11. Zucker, C. et al. On the three-dimensional structure of local molecular clouds. *Astrophys. J.* **919**, 35 (2021).
12. Lindegren, L. et al. Gaia Early Data Release 3 – the astrometric solution. *Astron. Astrophys. Suppl. Ser.* **649**, A2 (2021).
13. Pelgrims, V., Ferrière, K., Boulanger, F., Lallement, R. & Montier, L. Modeling the magnetized Local Bubble from dust data. *Astron. Astrophys.* **636**, A17 (2020).
14. Welsh, B. Y., Sfeir, D. M., Sirk, M. M. & Lallement, R. EUV mapping of the local interstellar medium: the Local Chimney revealed? *Astron. Astrophys.* **352**, 308–316 (1999).
15. Bialy, S. et al. The Per-Tau Shell: a giant star-forming spherical shell revealed by 3D dust observations. *Astrophys. J. Lett.* **919**, L5 (2021).
16. Alves, J. et al. A Galactic-scale gas wave in the solar neighbourhood. *Nature.* **578**, 237–239 (2020).
17. Großschedl, J. E., Alves, J., Meingast, S. & Herbst-Kiss, G. 3D dynamics of the Orion cloud complex – discovery of coherent radial gas motions at the 100-pc scale. *Astron. Astrophys. Suppl. Ser.* **647**, A91 (2021).
18. Perrot, C. A. & Grenier, I. A. 3D dynamical evolution of the interstellar gas in the Gould Belt. *Astron. Astrophys. Suppl. Ser.* **404**, 519–531 (2003).
19. Dzib, S. A., Loinard, L., Ortiz-León, G. N., Rodríguez, L. F. & Galli, P. A. B. Distances and kinematics of Gould Belt star-forming regions with Gaia DR2 results. *Astrophys. J.* **867**, 151 (2018).
20. Kerr, R. M. P., Rizzuto, A. C., Kraus, A. L. & Offner, S. S. R. Stars with Photometrically Young Gaia Luminosities Around the Solar System (SPYGLASS). I. Mapping young stellar structures and their star formation histories. *Astrophys. J.* **917**, 23 (2021).
21. Maíz-Apellániz, J. The origin of the Local Bubble. *Astrophys. J. Lett.* **560**, L83–L86 (2001).
22. El-Badry, K., Ostriker, E. C., Kim, C.-G., Quataert, E. & Weisz, D. R. Evolution of supernovae-driven superbubbles with conduction and cooling. *Mon. Not. R. Astron. Soc.* **490**, 1961–1990 (2019).
23. Inutsuka, S.-I., Inoue, T., Iwasaki, K. & Hosokawa, T. The formation and destruction of molecular clouds and galactic star formation. An origin for the cloud mass function and star formation efficiency. *Astron. Astrophys.* **580**, A49 (2015).
24. Dawson, J. R. The supershell–molecular cloud connection: large-scale stellar feedback and the formation of the molecular ISM. *Publ. Astron. Soc. Aust.* **30**, e025 (2013).
25. Cox, D. P. & Smith, B. W. Large-scale effects of supernova remnants on the Galaxy: generation and maintenance of a hot network of tunnels. *Astrophys. J. Lett.* **189**, L105–L108 (1974).
26. McKee, C. F. & Ostriker, J. P. A theory of the interstellar medium: three components regulated by supernova explosions in an inhomogeneous substrate. *Astrophys. J.* **218**, 148–169 (1977).
27. Kim, C.-G., Ostriker, E. C. & Raileanu, R. Superbubbles in the multiphase ISM and the loading of Galactic winds. *Astrophys. J.* **834**, 25 (2017).

Methods

Deriving stellar cluster properties

In Extended Data Table 1, we summarize the properties of young stellar clusters used in this work. Our sample includes young clusters out to approximately 300–400 pc, up to a maximum age of 20 Myr. Our sample is chosen to provide optimal coverage of all young (<5 Myr) clusters associated with star-forming regions currently lying on the surface of the Local Bubble, including the Lupus[28], Ophiuchus[29], Chamaeleon[30], Corona Australis[31] and Taurus Molecular Clouds[32]. In addition to the youngest stellar populations on the Local Bubble's surface, several recent studies provide evidence that at least two of the surface clouds—Taurus[32] and Ophiuchus[29]—exhibit multiple generations of star formation, with an older stellar population (>5 Myr) existing alongside the younger one. For these clouds, we include both young and old populations. Older stellar populations in the Scorpius Centaurus[33,34] association—Upper Centaurus Lupus, Lower Centaurus Crux and Upper Scorpius—are likewise included in Extended Data Table 1. Although many of the known moving groups (for example, Beta Pic, Octans and Carina[33]) also lie inside the bubble, their ages (>25 Myr) are larger than the bubble's estimated age and are thus excluded from our analysis[33]. Finally, we also include clusters beyond the Local Bubble but associated with star-forming regions along the Radcliffe Wave and the Split, including the Perseus[35], Orion[17] and Serpens[36] Molecular Clouds.

We rely on existing studies (Extended Data Table 1) to determine stellar membership of each cluster, but we only include stars that are detected in the *Gaia* EDR3 catalogue. We uniformly associate stellar members of each cluster with *Gaia* EDR3 using a crossmatch radius of 1" to obtain its sky coordinates, parallax and proper motions. If radial velocities for the stars are provided along with the target selection in their original publication, we adopt those existing radial velocities in our analysis, some of which are obtained with high-quality ground-based near-infrared spectroscopy. Otherwise, if no radial velocity data are provided, we use the *Gaia* radial velocities and restrict our analysis to only those stars that also have a *Gaia* radial velocity detection. We largely rely on the sample selection outlined in each cluster's original publication to filter outliers, many of which are defined using *Gaia* DR2 data. However, as an additional constraint, we require that all stars must have a parallax over error greater than two and small renormalized unit weight error (RUWE < 1.4)[37]. We also require the radial velocity error to be <5 km s^{-1}, a relatively generous cut chosen because our algorithm incorporates the errors on the individual stellar measurements when determining the mean cluster motion. After applying all of these cuts, we perform a sigma-clipping procedure using the astropy[38] package, removing extreme outliers whose radial velocities are inconsistent with the rest of the cluster population at the 3σ level. Finally, we require that each cluster have at least three stellar members. The mean stellar membership is much higher than this, averaging 37 stars per cluster.

To transform the sky coordinates (right ascension α and declination δ), parallax (π), proper motions (μ_{RA}, μ_{DEC}) and heliocentric radial velocities (v_{helio}) of members to an average 3D space position and 3D velocity of the cluster in a Heliocentric Galactic Cartesian reference frame (x, y, z, U, V, W), we use the extreme deconvolution algorithm[39]. The extreme deconvolution algorithm infers an n-dimensional distribution function using a Gaussian mixture model given the presence of noisy, incomplete and heterogeneous samples of the underlying population. We apply the algorithm to infer the average 6D phase information of each cluster, given the observed values and estimated error covariances of its stellar members. For each star we use the astropy[38] functionality within galpy[40] to compute the star's Heliocentric Galactic Cartesian coordinates (x, y, z) and associated space motions (U, V, W) given the observed *Gaia* quantities (α, δ, π, μ_{RA}, μ_{DEC}, v_{helio}). We assume U points towards the Galactic centre, V points towards the direction of Galactic rotation and W points towards the North Galactic Pole. To accurately estimate errors on (x, y, z, U, V, W) for each star, we randomly sample 100 times from a multi-dimensional Gaussian in ($\alpha, \delta, \pi, \mu_{RA}, \mu_{DEC}, v_{helio}$) space assuming Gaussian uncertainties on all parameters as reported in the *Gaia* EDR3 catalogue. Transforming each sample to a Heliocentric Galactic Cartesian coordinate frame, we then calculate the covariance of the set of samples for each star. Feeding the set of (x, y, z, U, V, W) values for the individual stellar cluster members and their associated sample covariances into the extreme deconvolution algorithm, we obtain the mean and variance of a single 6D Gaussian defining the average 3D position and 3D space motion of each cluster, as shown in Extended Data Table 1. We adopt a peculiar solar motion of ($U_\odot$, $V_\odot$, $W_\odot$) = (10.0, 15.4, 7.8) km s^{-1} (ref. [41]) and correct the (U, V, W) values of each cluster for this solar motion to obtain its current 3D space velocity with respect to the LSR frame (U_{LSR}, V_{LSR}, W_{LSR}). We use the mean cluster motion to 'traceback' its trajectory in the Galaxy. To 'traceback' a cluster means to compute the 3D position and 3D motion that the cluster would have had at different times in the past, given estimates of its present 3D position and 3D motion. In practice, the full bound orbit of the cluster can be computed, and the small section of the orbit constituting its trajectory in the recent past is extracted.

We perform the dynamical traceback of each cluster using the galpy package[40], which supports orbit integrations in a Milky Way-like potential, consisting of a bulge, disk and dark matter halo. We sample the orbit from −20 Myr to the present day. Alongside each cluster, we also trace the Sun's orbit backwards in time over the past 20 Myr and correct each cluster's orbit for the Sun's peculiar motion to ensure all orbits remain in the LSR frame. We emphasize that galpy only accounts for the gravitational potential of the Galaxy and does not consider the gravitational effects of the parental gas clouds in which many of these clusters are embedded. However, given the large extent of the Local Bubble relative to any individual star-forming region and the fact that the Galactic potential should dominate over the gravity of any local gas, galpy still serves as a useful probe of the dynamics of the Local Bubble. This argument is bolstered by recent results from numerical simulations, which indicate that stellar orbits can be recovered with high fidelity up to 20 Myr in the past, even without explicitly modelling non-axisymmetric components of the potential[42]. The dynamical tracebacks for all clusters in Extended Data Table 1 are publicly available at the Harvard Dataverse (https://doi.org/10.7910/DVN/E8PQOD).

Modelling the Local Bubble's expansion

In this section, we derive an analytic model for the radius and expansion velocity of the Local Bubble as a function of time, using constraints provided by the dynamical traceback data summarized in Extended Data Tables 1 and 2 (see the Data Availability section to access the full traceback data on each cluster). The results of this section underpin our model for the temporal evolution of the Local Bubble shown in Fig. 2 (static version) and Supplementary Fig. 2 (interactive version).

To model the expansion of the Local Bubble, we use recent literature that leverages one-dimensional spherically symmetric hydrodynamic simulations using the Athena++ code to study the dynamical evolution of superbubbles driven by clustered supernovae in a uniform medium[22]. Specific treatment is given to the effects of cooling at the shell–bubble interface. Building on this recent literature, we adopt an analytic model[22] describing the radius, R, of the superbubble's expanding shell as a function of time t since its birth, parameterized by the ambient density n_0 of the interstellar medium, the cooling efficiency at the shell's surface θ, the time separation between supernovae explosions Δt_{SNe} within the cluster powering its formation, and the energy input per supernova explosion E_{SN}, as follows:

$$R(t) = 83\ \text{pc} \times (1-\theta)^{\frac{1}{5}} \left(\frac{E_{\text{SN}}}{10^{51}\text{erg}}\right)^{\frac{1}{5}} \left(\frac{\Delta t_{\text{SNe}}}{0.1\ \text{Myr}}\right)^{\frac{-1}{5}} \left(\frac{n_0}{1\ \text{cm}^{-3}}\right)^{\frac{-1}{5}} \left(\frac{t}{1\ \text{Myr}}\right)^{\frac{3}{5}} \quad (1)$$

At any time t the (x, y, z) coordinates of the surface of this expanding spherical shell, centred on $(x_{\text{cen}}, y_{\text{cen}}, z_{\text{cen}})$, corresponding to the epicentre of the supernova explosions, can be parameterized as:

$$(x(t) - x_{\text{cen}})^2 + (y(t) - y_{\text{cen}})^2 + (z(t) - z_{\text{cen}})^2 = R(t)^2 \quad (2)$$

The 3D positions of each cluster at birth (derived from the dynamical tracebacks given the cluster's age) provide a constraint on the bubble's radius as a function of time. So, under the assumption that the formation of the young stars listed in Extended Data Table 2 was triggered by the shell's expansion, we can infer the parameters governing the Local Bubble's evolution using this analytic framework. We emphasize that this theoretical formalism is an approximation of the bubble's true morphology. We do not actually expect the bubble to expand spherically because the interstellar medium is highly turbulent with density fluctuations. Indeed, the Local Bubble today is observed to have a complex, non-spherical morphology. Extended Data Table 2 lists the 3D (x, y, z) birth positions for the subset of young clusters used to model the bubble expansion in the LSR frame, given their stellar tracebacks and estimated ages.

As several of the parameters governing the superbubble's evolution are degenerate, we make a number of simplifying assumptions. Previous work[6,7,21] estimates that 14–20 supernovae in the UCL and LCC stellar groups over the past approximately 13 Myr have together created the Local Bubble. The formalism of the analytic superbubble model assumes that all supernovae are driven from a single location. Rather than model each individual supernova explosion given the tracebacks of UCL and LCC, we assume that the epicentre of the explosion $(x_{\text{cen}}, y_{\text{cen}}, z_{\text{cen}})$ lay equidistant between UCL and LCC at the time of the first explosion, t_{exp}. This approximation is justified as UCL and LCC lay roughly co-spatial at early times, when the most powerful supernovae driving the superbubble's expansion would have gone off. We leave the time of the first supernova explosion, t_{exp}, as a free parameter in our model. The subsequent evolution of the Local Bubble is governed by t_{exp} and equation (1). We assume a fixed energy input per supernova of 10^{51} erg. We also assume a fixed cooling efficiency θ of 0.7. However, we test a variety of cooling efficiencies, ranging from 0.4 to 0.9, and find that fixing the cooling efficiency to a value of 0.7 does not affect our estimate for the time of the first explosion, and only has a modest effect on the ambient density and duration between supernovae (with the variation falling within our reported uncertainties on these parameters, as we will later show in Extended Data Fig. 1).

Having fixed the cooling efficiency and energy input per supernova, the free parameters of our model include the ambient density, n_0, the time separation between supernova explosions, Δt_{SNe}, and the time of the first supernova explosion, t_{exp}. We infer the values of n_0, Δt_{SNe} and t_{exp} in a Bayesian framework. We assume that the density of the shell has a Gaussian profile with an uncertainty (or thickness) of Δ_R, which corresponds to a log-likelihood of the following form:

$$\log(L) = \frac{-1}{2} \sum_{i=1}^{n} \left[\ln(2\pi\Delta_R{}^2) + \frac{[R(t_i, n_0, \Delta t_{\text{SNe}}) - r_i(t_i)]^2}{\Delta_R{}^2} \right] \quad (3)$$

Here the $R(t_i, n_0, \Delta t_{\text{SNe}})$ term is the radius of the Local Bubble's expanding shell governed by equations (1) and (2), evaluated at time t_i, corresponding to the difference between the time at which the ith cluster was born and the time of the first explosion ($t_i = t_{\text{birth},i} - t_{\text{exp}}$). The Local Bubble's shell with radius $R(t_i)$ is centred on $(x_{\text{cen}}, y_{\text{cen}}, z_{\text{cen}})$, derived from the mean 3D position of UCL and LCC in the LSR at time t_{exp}, when the first supernova went off in UCL or LCC. The $r(t_i)$ term is the radius of a sphere with the same centre as $R(t_i)$, such that the ith cluster born at traceback time t_i lies on its surface, with coordinates of:

$$(x(t_i) - x_{\text{cen}})^2 + (y(t_i) - y_{\text{cen}})^2 + (z(t_i) - z_{\text{cen}})^2 = r(t_i)^2 \quad (4)$$

Finally, the Δ_R term in the log-likelihood given in equation (3) should be interpreted as an error term, encompassing uncertainties in both the ages of the clusters and on their mean (U_{LSR}, V_{LSR}, W_{LSR}) motions. We infer Δ_R to be an additional free parameter in our model. The total log-likelihood of all n clusters is the sum of their individual log-likelihoods, evaluated at the respective time of their births, which will be optimized when the difference between $R(t_i)$ and $r(t_i)$ is minimized.

Using the log-likelihood in equation (3), we sample for the values of t_{exp}, n_0, Δt_{SNe} and Δ_R using the nested sampling code dynesty[43]. For t_{exp}, we adopt a truncated normal prior with a mean of −13 Myr and a s.d. of 1 Myr over the range of −16 Myr to −10 Myr (refs. [6,21]; consistent with previous evolutionary synthesis models of UCL and LCC). For n_0, we adopt a truncated log-normal prior with a mean of 2 cm^{-3} and a s.d. of a factor of two over the range of 0.1 to 10 cm^{-3}, consistent with the density range explored in the Athena++ simulations underpinning the expansion model[22]. For Δt_{SNe}, we adopt a truncated log-normal prior with a mean of 0.8 Myr and a s.d. of a factor of two, over the range of 0.05 Myr to 3 Myr (ref. [7]; consistent with previous estimates of approximately 16 supernovae occurring in UCL and LCC over the past 13 Myr). Finally, guided by the typical errors on the 3D motions (a few kilometres per second) and the ages (a few megayears), we adopt a truncated normal prior on Δ_R, with a mean of 15 pc and a s.d. of 5 pc, over the range of 0 to 30 pc. We run with the default parameters of dynesty's dynamic nested sampler.

The results of our sampling procedure are summarized in Extended Data Fig. 1. We find a median value and 1σ errors (computed using the 16th, 50th and 84th percentiles of the samples) of $\Delta t_{\text{SNe}} = 1.06^{+0.63}_{-0.39}$ Myr, $n_0 = 2.71^{+1.57}_{-1.02}$ cm^{-3}, $t_{\text{exp}} = -14.39^{+0.78}_{-0.74}$ Myr and $\Delta_{\text{R}} = 23.31^{+2.54}_{-2.29}$ pc. The best-fit model corresponds to an epicenter of the bubble of $(x_{\text{cen}}, y_{\text{cen}}, z_{\text{cen}})$ = (39, 7, −18) pc in the LSR frame 14.4 Myr ago. Adopting these median parameters, a model for the evolution of the Local Bubble is overlaid in Fig. 2. We compute the radius of the Local Bubble's shell and its expansion velocity over its lifetime, as plotted in Extended Data Fig. 2a, b. On the basis of our model, and leveraging the full set of posterior samples, we estimate a present-day expansion speed of $6.7^{+0.5}_{-0.4}$ km s^{-1} and a radius of 165 ± 6 pc. This present-day expansion speed is consistent with the current range of 3D velocity magnitudes of stars at the surface of its shell (approximately 5–9 km s^{-1}), assuming that the rest velocity of the shell lies within a few kilometres per second of the LSR (as we expect it to, as the LSR is currently inside the Local Bubble).

However, as illustrated in Extended Data Fig. 1, there is a strong covariance between Δt_{SNe} and n_0 such that an increase in the density of the ambient medium can be compensated for by a decrease in the time between supernova explosions, and vice versa. Given the limitations of our modelling, we intend the superbubble evolution shown in Fig. 2 to only serve as a possible, idealized, example of how the Local Bubble could have reached its present-day morphology.

Potential origin of the Local Bubble

In this section, we seek to shed additional light on the origin of the Local Bubble, by using a momentum analysis to test whether UCL and LCC harboured enough supernovae to excavate a cavity the size of the Local Bubble. To do so, we compute the momentum of the Local Bubble's shell from its current expansion velocity (calculated in the previous section and shown in Extended Data Fig. 2) and estimates of its mass (obtained from 3D dust mapping). We can then further build

on the analytic superbubble model constrained above to obtain the expected average momentum injection per supernova, $\hat{p}$. The ratio of the total momentum of the shell to the average momentum injected per supernova provides a constraint on the number of supernovae required to power its expansion, which can then be compared with existing estimates for how many supernovae have gone off in UCL and LCC based on population synthesis modelling[7,21].

To obtain the momentum of the shell, we calculate its swept-up mass $M_{\rm shell}$ by integrating the 3D volume density derived from the 3D dust map[9] between a distance of $[R_{\rm shell}, R_{\rm shell}+R_{\rm thickness}]$ from the Sun and multiplying by the mean particle mass $\langle m\rangle = 1.4m_{\rm H}$, where $m_{\rm H}$ is the mass of a proton and the factor of 1.4 corrects for the helium abundance. $R_{\rm shell}$ is the boundary (that is, inner radius) of the Local Bubble (shown in Fig. 1) and $R_{\rm thickness}$ is the shell's thickness, such that $R_{\rm shell}+R_{\rm thickness}$ corresponds to the outer radius. The Local Bubble model we use estimates $R_{\rm thickness}$ to be between 50 and 150 pc (ref. [13]), which is quite large, but encompasses the full depth of structure currently lying on the bubble's surface.

Adopting $R_{\rm thickness}$ = 100 pc with an estimated 1σ uncertainty of 50 pc, we obtain $M_{\rm shell} = 1.4^{+0.65}_{-0.62}\times10^6 M_\odot$ for the swept-up mass. To estimate the current expansion velocity of the Bubble $v_{\rm exp}$, we leverage the posterior samples from our model describing the Local Bubble's evolution (fit to the dynamical tracebacks; Extended Data Fig. 1) to evaluate the velocity of the shell $v_{\rm shell} = {\rm d}R/{\rm d}t$ in the present day (Extended Data Fig. 2). Doing so, we obtain $v_{\rm exp} = 6.7^{+0.5}_{-0.4}$ km s^{-1}. To propagate uncertainties throughout this section, we use the full set of posterior samples when leveraging parameters from the expansion model. To propagate uncertainties on the observed swept-up mass of the shell, we draw the same number of samples from a Gaussian with a mean of $M_{\rm shell} = 1.4\times10^6 M_\odot$ and a s.d. of $6\times10^5 M_\odot$. Whenever uncertainties are reported, we use the 16th, 50th and 84th percentiles of the samples to compute the median and 1σ error bounds. Given samples for the current expansion velocity and swept-up mass, the corresponding momentum of the Local Bubble's shell is:

$$p_{\rm shell} = M_{\rm shell}\times v_{\rm exp} = 9.6^{+4.4}_{-4.1}\times10^6 M_\odot\ {\rm km\,s^{-1}} \quad (5)$$

In the previous section, we used an analytic superbubble expansion model[22] to constrain the temporal evolution of the Local Bubble's size and velocity. The same simulations underpinning this formalism indicate that the average momentum injected per supernovae $\hat{p}$ depends on the same free parameters, namely the energy input per supernova explosion, $E_{\rm SN}$, the cooling efficiency, θ, the duration between supernova explosions, $\Delta t_{\rm SNe}$, the density of the ambient medium, n_0, and time, t:

$$\hat{p}(t) = 4\times10^5 M_\odot\ {\rm km\ s^{-1}}(1-\theta)^{\frac{4}{5}}\left(\frac{E_{\rm SN}}{10^{51}\ {\rm erg}}\right)^{\frac{4}{5}}\left(\frac{\Delta t_{\rm SNe}}{0.1\ {\rm Myr}}\right)^{\frac{1}{5}}\left(\frac{n_0}{1\ {\rm cm^{-3}}}\right)^{\frac{1}{5}}\left(\frac{t}{1\ {\rm Myr}}\right)^{\frac{2}{5}} \quad (5)$$

Therefore, we again fix θ = 0.7 and $E_{\rm SN} = 10^{51}$ erg, and leverage the samples of $\Delta t_{\rm SNe}$, n_0 and $t_{\rm exp}$. We evaluate $\hat{p}$ over the lifetime of each realization of the bubble and draw a random sample of $\hat{p}$ from each distribution. We then take the 16th, 50th and 84th percentiles of the random samples drawn from all realizations (Extended Data Fig. 1) to obtain a mean value and 1σ uncertainties on the average momentum injected per supernova $\hat{p}$:

$$\hat{p} = 6.5^{+1.6}_{-2.4}\times10^5 M_\odot\ {\rm km\ s^{-1}}$$

Finally, dividing all samples of $p_{\rm shell}$ by all samples of $\hat{p}$ we obtain:

$$N_{\rm SNe} = p_{\rm shell}/\hat{p} = 15^{+11}_{-7}\ \text{supernovae}$$

The marginal distribution of $N_{\rm SNe}$ is shown in Extended Data Fig. 3. The average number of 15^{+11}_{-7} supernovae is in good agreement with previous results[6,7,21], which argue that UCL and LCC have produced 14–20 supernovae over their lifetimes based on an analysis of their current stellar membership and modelling of a Salpeter[44] initial mass function.

Consistent with this physical scenario, before supernovae start going off in UCL and LCC, our model predicts a typical ambient density of the interstellar medium of $n_0 = 2.71^{+1.57}_{-1.02}$ cm^{-3}. Assuming that the volume of the sphere with a radius of 165 ± 6 pc (our current estimate for the radius of the Local Bubble from the analytic expansion model) is uniformly filled with a gas density of $n_0 = 2.71^{+1.57}_{-1.02}$ cm^{-3}, we would expect $1.7^{+0.97}_{-0.63}\times10^6 M_\odot$ of gas to be displaced and swept up into its surrounding shell over its lifetime. Using the 3D dust measurements, we measure an actual swept-up mass of $M_{\rm shell} = 1.4^{+0.65}_{-0.62}\times10^6 M_\odot$ on the surface of the Local Bubble, aligned with this estimate of $1.7\times10^6\ M_\odot$.

Given uncertainties in the exact volume density of gas and dust inside the bubble traced by 3D dust, with some recent work suggesting that there is only a modest drop in volume density coincident with the cavity of hot ionized gas[45], we note that these momentum calculations (and, more broadly, the analytic superbubble expansion model) are largely insensitive to the exact difference in density interior and exterior to the bubble's boundary. The analytic expansion model we adopt[22] includes the ambient density of the interstellar medium at the time of the first supernova explosion as a free parameter; however, this ambient density parameter is constrained using the dynamical traceback data (not the 3D dust maps) and does not require any explicit assumptions about the exact density interior and exterior to the bubble as the shell expands. Similarly, even though the swept-up mass calculation does depend on 3D dust mapping[9], the mass is only measured within the denser shell of neutral gas and dust (where the uncertainties in the underlying dust extinction are smaller) and has no dependence on the density in the hot inner cavity, which could be subject to larger uncertainties due to the very low levels of dust extinction.

The stellar tracebacks of UCL/LCC and the peculiar motion of the Sun

Tracebacks of the average stellar cluster motions are expressed relative to the LSR, which itself depends on the measured motion of the Sun. Even in the age of *Gaia*, the Sun's exact motion in the Galaxy is uncertain, especially along the '*Y*' direction (along Galactic rotation). In this paper, we revise estimates of the tracebacks of the UCL and LCC clusters from previous literature[6,7], which presents arguments that UCL and LCC were born outside of the present-day boundary of the Local Bubble even though their members were the likely progenitors of the Local Bubble. In this section, we revisit these extant stellar traceback calculations from previous work[6,7] finding that a revised calculation places UCL and LCC near the centre of the Local Bubble when they formed.

Although previous studies[21] have proposed UCL and LCC as the likely progenitor population, the previous study in question[6] is the first to perform an unbiased stellar search of all nearby B stars to track down the remains of OB associations hosting supernovae capable of powering the Local Bubble. This previous study[6] confirms that UCL and LCC are the only populations capable of having powered the Local Bubble, but, after tracing back the stellar members, find that both UCL and LCC formed >100 pc outside the present-day boundary of the Local Bubble. Extended Data Figure 4a shows the extant stellar traceback results, in which UCL and LCC only lay interior to the present-day boundary of the Local Bubble during the past few megayears[6]. The authors of the previous study[6] noted this potential inconsistency (how does a supernova cause a bubble it does not lie within?), but they argue that the location of the UCL and LCC clusters with respect to the centre of the bubble is not crucial.

The previous study[6], which places UCL and LCC outside the bubble, uses Hipparcos parallaxes and proper motions with radial velocities collected from the literature to derive the (*U*, *V*, *W*) 3D space motion of

each member. In the previous study[6], using the (U, V, W) value of each individual star, the authors calculate the mass–weighted mean (U, V, W) velocity of all members of UCL and LCC, and then assign this group 3D (U, V, W) space velocity to each individual stellar member for the purposes of performing the tracebacks. The authors of this previous literature[6] also state that they correct the mean 3D group velocity for the Sun's peculiar motion, adopting a value of ($U_\odot$, $V_\odot$, $W_\odot$) = (10.0, 5.2, 7.2) km s^{-1} (ref. [46]), so that the traceback of each star is reported in the LSR frame.

As a first step, we attempt to reproduce the original results from previous literature[6] (Extended Data Fig. 4a) using their own data. Specifically, we calculate the mass-weighted mean velocity of the UCL and LCC stars from their Table A1 (ref. [6]) and their equation (2) (ref. [6]), finding (U, V, W = −7.1 −20.6, −5.8) km s^{-1} without correcting for the solar motion. With a value for the Sun's peculiar motion of (10.0, 5.2, 7.2) km s^{-1} (ref. [46]) used in the previous literature, these values translate to ($U_{\rm LSR}$, $V_{\rm LSR}$, $W_{\rm LSR}$ = 2.9, −15.4, 1.4) km s^{-1} in the LSR frame. Extended Data Figure 4b shows the dynamical tracebacks we calculate in galpy (Methods) from the Table A1 data from the previous literature[6] and with the value for the Sun's peculiar motion of (10.0, 5.2, 7.2) km s^{-1} (ref. [46]). Using the default orbit integrator in galpy with its standard Milky Way potential[40], we are unable to reproduce the results from previous literature, particularly the strong curvature in the tracebacks along the +X direction. The previous literature[6] uses an epicyclic approximation for the stars' motions (see their Section 2), which may be responsible for part of the discrepancy. This systematic smearing out of the tracebacks towards +X in their Fig. 2 (ref. [6]) manifests in the entire sample of B stars and is not isolated to UCL and LCC.

In examining the stellar motions of UCL and LCC, we find that the choice of the solar peculiar motion—necessary to convert to the LSR frame—has a non-negligible effect on where the birthplaces of UCL and LCC lie with respect to the centre of the Local Bubble. There have been dozens of attempts to constrain the Sun's peculiar motion, but $V_\odot$ (the motion in the direction of Galactic rotation, along Y) remains highly uncertain: current estimates range between $V_\odot$ = 4 and $V_\odot$ = 16 km s^{-1} (ref. [47]).

The value of $V_\odot$ = 5.2 km s^{-1} (ref. [46]) adopted in previous literature[6,7] is one of the lowest values of $V_\odot$. As Extended Data Fig. 4c shows, if we use the same Hipparcos data used in the previous literature but replace their value for $V_\odot$ (5.2 km s^{-1}; ref. [46]) with a value of 15.4 km s^{-1} (ref. [41]), we find that UCL and LCC are born near the bubble's centre. Extended Data Figure 4d shows that updating the Hipparcos data with *Gaia* data and adopting the same peculiar motion used in this work[41] makes almost no difference to the tracebacks, suggesting that the uncertainty in the Sun's peculiar motion is the dominant source of uncertainty in determining the birth location of UCL and LCC. We adopt a value of 15.4 km s^{-1} (ref. [41]) when calculating all of the tracebacks in this paper, which is towards the upper end of estimates for $V_\odot$. Given the large uncertainty on $V_\odot$, we have tested the robustness of our results to the choice of solar peculiar motion and find that any motion for $V_\odot \gtrsim 10$ km s^{-1} is entirely consistent with the physical scenario we propose here. This $V_\odot$ = 10–16 km s^{-1} range encompasses the vast majority of estimates for $V_\odot$ used in the field today[47–50].

Data availability

The datasets generated and/or analysed during the current study are publicly available on the Harvard Dataverse (https://dataverse.harvard.edu/dataverse/local_bubble_star_formation/), including Extended Data Table 1 (https://doi.org/10.7910/DVN/ZU97QD), Extended Data Table 2 (https://doi.org/10.7910/DVN/1VT8BC), per-star data for individual stellar cluster members (https://doi.org/10.7910/DVN/1UPMDX) and the cluster tracebacks (https://doi.org/10.7910/DVN/E8PQOD).

Code availability

The results generated in this work are based on publicly available software packages and do not involve the extensive use of custom code. Given each star's reported *Gaia* data, we use the astropy[38] package to obtain the Heliocentric Galactic Cartesian positions and velocities. The extreme deconvolution algorithm in the astroML[51] package is used to estimate the mean 3D positions and velocities of the stellar clusters. The Orbit functionality in the galpy[40] package is used to perform the dynamical tracebacks. The dynesty[43] package is used to fit the analytic superbubble expansion model and determine the best-fit parameters governing the Local Bubble's evolution.

28. Galli, P. A. B. et al. Lupus DANCe. Census of stars and 6D structure with Gaia-DR2 data. *Astron. Astrophys.* **643**, A148 (2020).
29. Grasser, N. et al. The ρ Oph region revisited with Gaia EDR3. *Astron. Astrophys.* **652**, A2 (2021)
30. Galli, P. A. B. et al. Chamaeleon DANCe. Revisiting the stellar populations of Chamaeleon I and Chamaeleon II with Gaia-DR2 data. *Astron. Astrophys.* **646**, A46 (2021).
31. Galli, P. A. B. et al. Corona-Australis DANCe. I. Revisiting the census of stars with Gaia-DR2 data. *Astron. Astrophys.* **634**, A98 (2020).
32. Krolikowski, D. M., Kraus, A. L. & Rizzuto, A. C. Gaia EDR3 reveals the substructure and complicated star formation history of the Greater Taurus-Auriga star-forming complex. *Astron. J.* **162**, 3 (2021).
33. Gagné, J. & Faherty, J. K. BANYAN. XIII. A first look at nearby young associations with Gaia Data Release 2. *Astrophys. J.* **862**, 138 (2018).
34. Gagné, J. et al. BANYAN. XI. The BANYAN Σ multivariate Bayesian algorithm to identify members of young associations with 150 pc. *Astrophys. J.* **856**, 23 (2018).
35. Ortiz-León, G. N. et al. The Gould's Belt Distances Survey (GOBELINS). V. Distances and kinematics of the Perseus Molecular Cloud. *Astrophys. J.* **865**, 73 (2018).
36. Herczeg, G. J. et al. An initial overview of the extent and structure of recent star formation within the Serpens molecular cloud using Gaia Data Release 2. *Astrophys. J.* **878**, 111 (2019).
37. Fabricius, C. et al. Gaia Early Data Release 3 – catalogue validation. *Astron. Astrophys. Suppl. Ser.* **649**, A5 (2021).
38. The Astropy Collaboration. The Astropy Project: building an open-science project and status of the v2.0 Core Package*. *Astron. J. Supp.* **156**, 123 (2018).
39. Bovy, J., Hogg, D. W. & Roweis, S. T. Extreme deconvolution: inferring complete distribution functions from noisy, heterogeneous and incomplete observations. *Ann. Appl. Stat.* **5**, 1657–1677 (2011).
40. Bovy, J. galpy: a Python library for Galactic dynamics. *Astrophys. J. Supp.* **216**, 29 (2015).
41. Kerr, F. J. & Lynden-Bell, D. Review of galactic constants. *Mon. Not. R. Astron. Soc.* **221**, 1023–1038 (1986).
42. Kamdar, H., Conroy, C. & Ting, Y.-S. Stellar streams in the Galactic disk: predicted lifetimes and their utility in measuring the galactic potential. Preprint at https://arxiv.org/abs/2106.02050v1 (2021).
43. Speagle, J. S. dynesty: a dynamic nested sampling package for estimating Bayesian posteriors and evidences. *Mon. Not. R. Astron. Soc.* **493**, 3132–3158 (2020).
44. Salpeter, E. E. The luminosity function and stellar evolution. *Astrophys. J.* **121**, 161 (1955).
45. Gontcharov, G. & Mosenkov, A. Interstellar polarization and extinction in the Local Bubble and the Gould Belt. *Mon. Not. R. Astron. Soc.* **483**, 299–314 (2019).
46. Dehnen, W. & Binney, J. J. Local stellar kinematics from Hipparcos data. *Mon. Not. R. Astron. Soc.* **298**, 387–394 (1998).
47. Francis, C. & Anderson, E. Calculation of the local standard of rest from 20574 local stars in the New Hipparcos Reduction with known radial velocities. *New Astron.* **14**, 615–629 (2009).
48. Wang, F. et al. Local stellar kinematics and Oort constants from the LAMOST A-type stars. *Mon. Not. R. Astron. Soc.* **504**, 199–207 (2021).
49. Reid, M. J. et al. Trigonometric parallaxes of high-mass star-forming regions: our view of the Milky Way. *Astrophys. J.* **885**, 131 (2019).
50. Schönrich, R., Binney, J. & Dehnen, W. Local kinematics and the local standard of rest. *Mon. Not. R. Astron. Soc.* **403**, 1829–1833 (2010).
51. VanderPlas, J., Connolly, A. J., Ivezić, Ž. & Gray, A. Introduction to astroML: machine learning for astrophysics. In *Proc. 2012 Conference on Intelligent Data Understanding* 47–54 (IEEE, 2012).

Acknowledgements The visualization, exploration and interpretation of data presented in this work were made possible using the glue visualization software, supported under NSF grant numbers OAC-1739657 and CDS&E:AAG-1908419. The interactive figures were made possible by the plot.ly python library. D.P.F. acknowledges support by NSF grant AST-1614941 'Exploring the Galaxy: 3-Dimensional Structure and Stellar Streams'. D.P.F., A.A.G. and C.Z. acknowledge support by NASA ADAP grant 80NSSC21K0634 'Knitting Together the Milky Way: An Integrated Model of the Galaxy's Stars, Gas, and Dust'. A.B. acknowledges support by the Excellence Cluster ORIGINS, which is funded by the German Research Foundation (DFG) under Germany's Excellence Strategy -EXC-2094-390783311. J.A. acknowledges support from the Data Science Research Centre and the TURIS Research Platform of the University of Vienna. J.G. acknowledges funding by the Austrian Research Promotion Agency (FFG) under project number 873708. C.Z. acknowledges that support for this work was provided by NASA through the NASA Hubble Fellowship grant number HST-HF2-51498.001 awarded by the Space Telescope Science Institute, which is operated by the Association of Universities for Research

in Astronomy, Inc., for NASA, under contract NAS5-26555. C.Z., A.A.G., J.A. and S.B. acknowledge Interstellar Institute's program 'The Grand Cascade' and the Paris-Saclay University's Institut Pascal for hosting discussions that encouraged the development of the ideas behind this work.

Author contributions C.Z. led the work and wrote the majority of the text. All authors contributed to the text. C.Z., A.A.G. and J.A. led interpretation of the observational results, aided by S.B., M.F. and A.B. who helped interpret their significance in light of theoretical models for supernova-driven star formation. C.Z. and A.A.G. led the visualization efforts. J.S.S. and D.P.F. helped shape the statistical modelling of the Local Bubble's expansion. C.Z., A.A.G. and J.S.S. contributed to the software used in this work. J.G. and C.S. provided data for and the subsequent interpretation of the 3D kinematics of the Orion region. D.K. helped to develop the code used to model the 3D positions and motions of stellar clusters described in the Methods.

Competing interests The authors declare no competing interests.

Additional information

Supplementary information The online version contains supplementary material available at https://doi.org/10.1038/s41586-021-04286-5.

Correspondence and requests for materials should be addressed to Catherine Zucker.

Peer review information *Nature* thanks Joanne Dawson and the other, anonymous, reviewer(s) for their contribution to the peer review of this work. Peer reviewer reports are available.

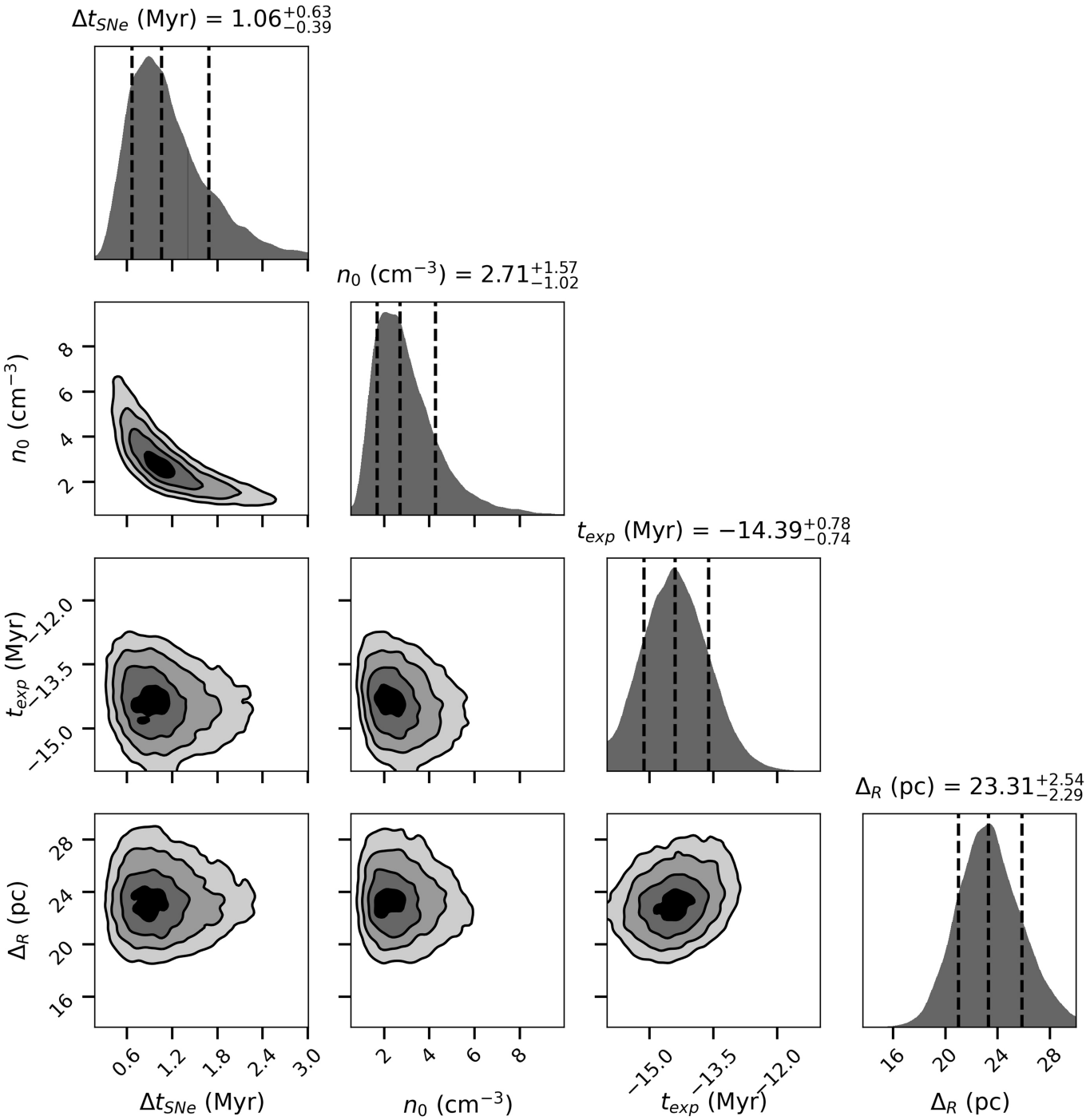

Extended Data Fig. 1 | 1D and 2D marginal distributions ("corner plot") of the model parameters governing the evolution of the Local Bubble's expanding shell. Parameters include the time since the first explosion (i.e. the age of the Local Bubble), t_{exp}, the density of the ambient medium the bubble is expanding into, n_0, the time between supernova explosions powering its growth, 𝞓t_{SNe}, and the thickness/uncertainty on the expanding shell radius 𝞓$_R$. In the 1D distributions, the vertical dashed lines denote the median and 1𝝈 errors, while in the 2D distributions, we show the 0.5𝝈, 1𝝈, 1.5𝝈, and 2𝝈 contours.

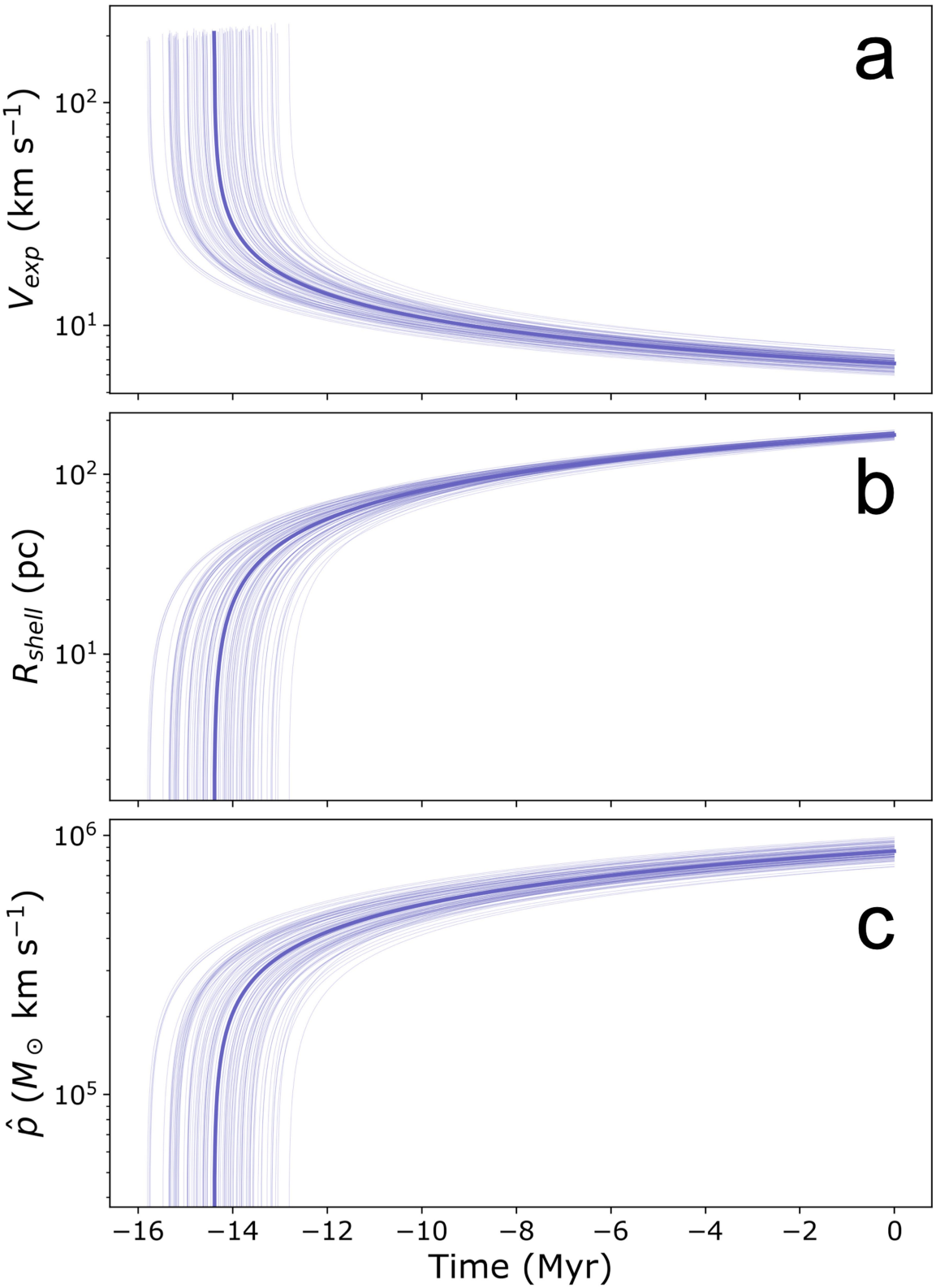

Extended Data Fig. 2 | Temporal evolution of the Local Bubble, based on the fit to the dynamical tracebacks and the analytic expansion model[22] summarized in the Methods section. Panel a) The evolution of the Local Bubble's expansion velocity v_{exp}. **Panel b)** The evolution of the Local Bubble's shell radius R_{shell}. **Panel c)** The evolution of the average momentum injection per supernova $\hat{p}$. The thick purple line represents the median fit, while the thin purple lines represent random samples. We estimate a current radius of 165±6 pc and current expansion velocity of $6.7^{+0.5}_{-0.4}$ km/s, corresponding to time t=0 Myr (the present day).

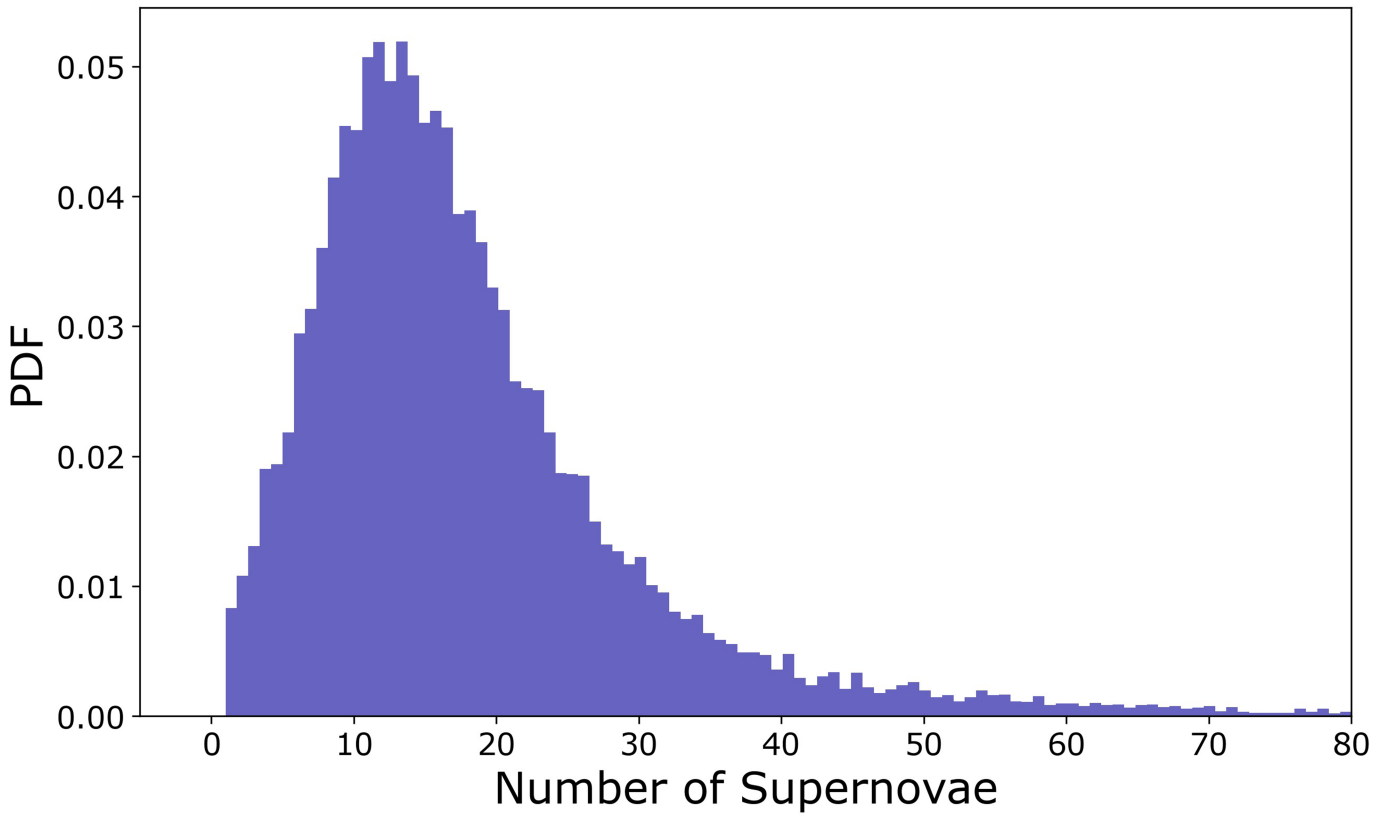

Extended Data Fig. 3 | PDF of the estimate of the number of supernovae required to power the Local Bubble's expansion. The estimate is obtained by comparing the shell's present-day momentum to the average momentum injected by supernovae.

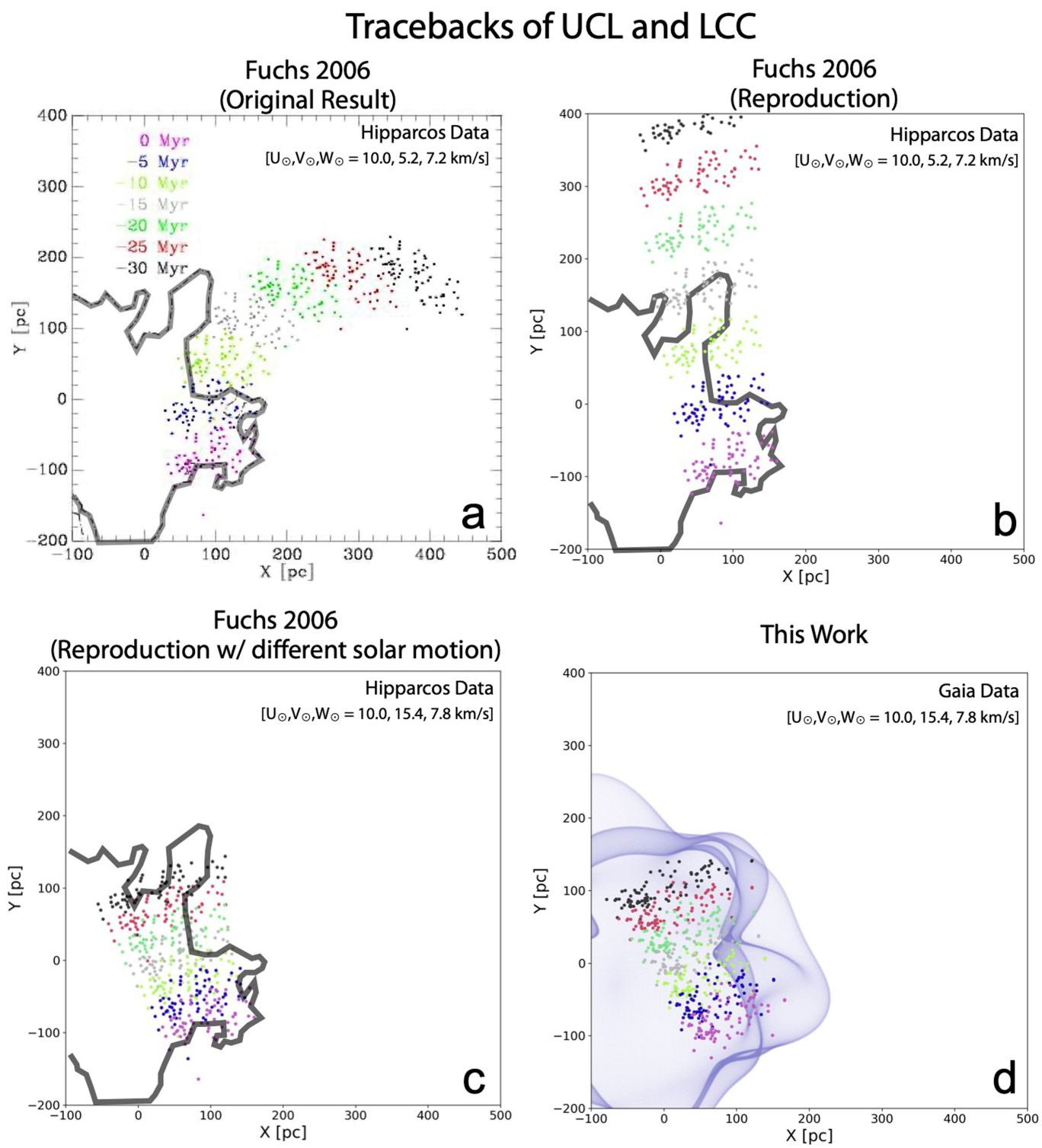

Extended Data Fig. 4 | Analysis of the stellar tracebacks of the UCL and LCC clusters, whose progenitors were likely responsible for the supernovae that created the Local Bubble. The scatter points indicate the positions of the current cluster members of UCL and LCC, which are colored as a function of time (spanning the present day in pink to 30 Myr ago in black). **Panel a:** Using Hipparcos data and adopting a solar peculiar motion $(U_\odot, V_\odot, W_\odot) = (10.0, 5.2, 7.2)$ km/s[46], previous literature[6,7] find that UCL and LCC were born outside the Local Bubble (black trace[4]) 15 Myr ago and only entered its present-day boundary in the past 5 Myr (reproduced from Fig. 6 in ref. [6]). **Panel b:** We attempt to reproduce the results from previous literature[6,7] using the same data and solar motion, but are unable to account for the curvature of the tracebacks, finding the UCL and LCC formed just inside its northern boundary 15 Myr ago. **Panel c:** Using a different value for the solar motion, $(U_\odot, V_\odot, W_\odot) = (10.0, 15.4, 7.8)$ km/s[41] but the same Hipparcos data, we find that UCL and LCC were born near the center of the Local Bubble. **Panel d:** Finally, using updated *Gaia* data but the same adopted solar motion used in panel c. $(U_\odot, V_\odot, W_\odot) = (10.0, 15.4, 7.8)$ km/s[41], we also find that UCL and LCC were born near the center of the bubble, given an updated model for its surface[13].

Extended Data Table 1 | Summary of the 3D positions and 3D velocities of young stellar clusters within 400 pc of the Sun

Cluster Region	Cluster Subgroup	Sample	N_{stars}	l	b	d	x	σ_x	y	σ_y	z	σ_z	U_{LSR}	σ_{ULSR}	V_{LSR}	σ_{VLSR}	W_{LSR}	σ_{WLSR}	Age
				°	°	pc	pc	pc	pc	pc	pc	pc	km/s	km/s	km/s	km/s	km/s	km/s	Myr
(1)	(2)	(3)	(4)	(5)	(6)	(7)	(8)	(9)	(10)	(11)	(12)	(13)	(14)	(15)	(16)	(17)	(18)	(19)	(20)
Perseus	NGC1333	Ortiz-Leon et al. 2018	28	158.3	-20.5	293	-255	9	101	3	-102	3	-7.2	0.9	5.0	1.2	-2.1	0.9	1
Perseus	IC348	Ortiz-Leon et al. 2018	126	160.5	-17.8	315	-282	8	100	3	-96	3	-6.9	1.0	9.6	0.9	0.1	0.9	3
Taurus	C2 - L1495	Krolikowski et al. 2021	24	168.9	-15.8	130	-122	2	24	1	-35	2	-6.0	0.5	3.2	0.7	-3.1	0.5	1
Taurus	C8 - B213	Krolikowski et al. 2021	12	170.9	-15.8	159	-151	4	24	2	-43	2	-7.9	0.3	2.4	0.5	0.7	0.2	3
Taurus	D4 - North	Krolikowski et al. 2021	21	172.3	-16.3	135	-128	25	17	7	-38	9	-4.9	2.9	5.2	5.9	-1.4	3.1	2
Taurus	C6 - L1524	Krolikowski et al. 2021	32	173.7	-15.5	128	-123	2	13	4	-34	1	-5.8	0.9	3.6	1.6	-1.9	0.9	2
Taurus	C7 - L1527	Krolikowski et al. 2021	11	174.0	-13.6	140	-136	3	14	1	-33	1	-5.9	1.3	4.0	0.7	-2.2	0.7	3
Taurus	C5 - L1546	Krolikowski et al. 2021	13	175.6	-16.5	162	-155	3	12	1	-45	1	-6.7	0.5	1.7	0.4	0.6	0.7	2
Taurus	D3 - South	Krolikowski et al. 2021	13	176.7	-18.0	122	-116	3	6	10	-37	7	-4.1	1.8	7.6	2.6	-2.0	0.8	6
Taurus	C1 - L1551	Krolikowski et al. 2021	14	179.1	-20.0	145	-136	2	2	1	-49	1	-5.1	1.7	0.3	0.7	0.5	1.1	2
Taurus	D2 - L1558	Krolikowski et al. 2021	13	179.9	-20.0	131	-123	29	0	8	-45	11	-5.0	2.5	4.3	5.2	-1.4	1.4	3
Taurus	D1 - L1544	Krolikowski et al. 2021	12	181.3	-7.3	172	-170	8	-3	5	-21	6	-8.9	0.6	1.5	1.7	-1.0	1.2	3
Taurus	C9 - 118TauEast	Krolikowski et al. 2021	4	184.0	-4.9	109	-109	2	-7	1	-9	2	-3.4	0.4	-3.4	0.2	-1.2	0.1	6
Orion	L1616	Großschedl et al. 2021	5	203.6	-24.6	382	-318	15	-139	6	-159	6	-8.8	2.7	4.7	1.1	-1.6	1.0	2
Orion	NGC2068/2071	Großschedl et al. 2021	44	205.2	-14.3	413	-362	10	-170	5	-102	3	-13.6	1.3	3.2	1.0	-0.5	1.3	2
Orion	NGC 2023/2024	Großschedl et al. 2021	37	206.6	-16.3	401	-344	10	-172	5	-112	3	-13.5	1.8	2.6	1.6	0.5	1.2	2
Orion	Sigma Ori	Großschedl et al. 2021	38	206.8	-17.3	401	-342	7	-173	4	-119	3	-16.3	1.0	-0.5	0.8	0.4	1.1	3
Orion	NGC1977	Großschedl et al. 2021	42	208.5	-19.1	393	-326	6	-177	3	-128	2	-15.1	1.3	-0.9	1.0	-1.1	1.1	3
Orion	Orion A, Head	Großschedl et al. 2021	241	209.2	-19.5	393	-324	9	-181	5	-131	4	-12.2	2.0	1.6	1.9	0.8	1.6	2
Orion	Orion A, Tail	Großschedl et al. 2021	153	211.8	-19.4	408	-327	17	-203	19	-135	8	-8.2	2.7	2.8	1.5	0.5	1.0	2
Chamaeleon	1-North	Galli et al. 2021	34	297.0	-14.8	192	84	1	-165	2	-49	1	-0.6	0.6	-3.8	0.7	-3.9	0.6	2
Chamaeleon	1-South	Galli et al. 2021	34	297.2	-15.8	188	82	2	-161	3	-51	2	-1.6	0.6	-4.2	1.1	-3.4	0.6	2
Sco-Cen	Lower Centaurus Crux, LCC	Gagne et al. 2018a,b	42	301.3	6.0	110	57	14	-93	13	11	15	1.9	1.5	-6.1	2.0	1.9	1.6	15
Chamaeleon	2	Galli et al. 2021	7	303.7	-14.4	196	105	2	-158	2	-48	2	-0.8	1.9	-3.2	3.3	-0.8	1.4	2
Sco-Cen	Upper Centaurus Lupus, UCL	Gagne et al. 2018a,b	40	330.7	13.3	129	109	25	-61	17	29	16	4.8	3.5	-4.6	1.9	2.7	1.4	16
Lupus	4	Galli et al. 2020	5	336.4	8.4	160	145	1	-63	1	23	1	5.2	1.5	-2.0	0.9	0.2	0.3	3
Lupus	3	Galli et al. 2020	27	339.5	9.4	158	146	2	-54	1	25	1	6.7	2.7	-2.0	1.3	0.2	0.9	3
Lupus	Off-Cloud Population	Galli et al. 2020	3	340.1	10.9	158	146	4	-52	1	29	5	5.8	3.6	-1.4	1.2	0.2	0.5	3
Sco-Cen	Upper Scorpius, USCO	Gagne et al. 2018a,b	43	351.4	22.0	142	130	8	-19	7	53	9	5.1	2.1	-0.8	1.2	0.9	1.7	10
Ophiuchus	Rho Oph, Population I	Grasser et al. 2021	96	353.1	17.2	138	131	3	-15	1	40	2	4.7	1.7	0.3	0.9	-1.4	1.0	1
Ophiuchus	Rho Oph, Population II	Grasser et al. 2021	32	353.9	18.3	139	131	6	-14	2	43	3	5.9	2.2	-0.4	1.3	1.8	0.8	10
Corona Australis	Off-Cloud Population	Galli et al. 2020	12	358.3	-13.7	146	141	3	-4	3	-34	4	3.9	2.2	-2.2	0.4	0.6	1.0	6
Corona Australis	On-Cloud Population	Galli et al. 2020	6	359.9	-16.7	149	143	3	0	1	-43	2	4.6	2.1	-1.4	0.4	-1.0	0.6	5
Serpens	Far South	Herczeg et al. 2019	3	27.3	2.4	384	341	3	176	0	16	0	12.3	2.6	1.9	1.7	-3.3	0.2	3

The rows are color-coded according to the cluster's longitude and map to the colors of the clusters shown in Figs. 1 and 2. **(1)** Name of the cluster region. **(2)** Name of the cluster subgroup. **(3)** Original publication forming the basis for stellar membership. **(4)** Number of stellar members used to estimate the average cluster properties. **(5)** Mean longitude **(6)** Mean latitude **(7)** Mean distance **(8-9)** Mean x position and x uncertainty in Heliocentric Galactic Cartesian coordinates. **(10-11)** Mean y position and y uncertainty in Heliocentric Galactic Cartesian coordinates. **(12-13)** Mean z position and z uncertainty in Heliocentric Galactic Cartesian coordinates. **(14-15)** Mean U motion and U uncertainty along the Heliocentric Galactic Cartesian x direction in the LSR frame. **(16-17)** Mean V motion and V uncertainty along the Heliocentric Galactic Cartesian y direction in the LSR frame. **(18-19)** Mean W motion and W uncertainty along the Heliocentric Galactic Cartesian z direction in the LSR frame. **(20)** Estimated age of the cluster drawn from the publication in column (3).

Extended Data Table 2 | Temporal evolution of cluster births at the surface of the Local Bubble's expanding shell

		Timestep (Myr)									
		-16	-15	-14	-10	-6	-5	-3	-2	-1	Now
		UCL Born	LCC Born	SNe in UCL/LCC Make Bubble	USCO and Oph "Old" Born	CrA, Taurus "Old" Born	CrA Born	Taurus "Young", Lupus Born	Taurus "Young", Cham Born	Taurus "Young", Oph "Young" Born	Dense Gas Enveloping Bubble
	UCL	(40,19,-24)	(44,14,-20)	(48,9,-17)	(64,-11,-3)	(81,-32,10)	(86,-37,14)	(95,-47,20)	(99,-51,23)	(104,-56,26)	(109,-61,29)
	LCC		(31,6,-18)	(32,0,-16)	(39,-27,-9)	(45,-54,0)	(47,-61,1)	(51,-74,5)	(53,-80,7)	(54,-87,9)	(57,-93,11)
	Rho Oph "Old" (Population II)				(75,-8,14)	(97,-11,28)	(102,-11,31)	(113,-12,37)	(119,-13,39)	(125,-13,41)	(131,-14,43)
	Upper Scorpius (USCO)				(83,-10,29)	(100,-14,42)	(105,-15,44)	(115,-17,49)	(119,-18,50)	(125,-18,52)	(130,-19,53)
	Taurus (D3 - South)					(-92,-40,-22)	(-96,-32,-25)	(-103,-16,-30)	(-107,-8,-33)	(-111,-1,-35)	(-116,6,-37)
	Corona Australis (Off-Cloud Population)					(120,9,-34)	(123,7,-34)	(130,2,-35)	(134,0,-35)	(137,-1,-35)	(141,-4,-34)
	Taurus (C9 - 118TauEast)					(-89,13,-1)	(-92,9,-2)	(-98,2,-5)	(-101,0,-6)	(-104,-4,-8)	(-109,-7,-9)
	Corona Australis (On-Cloud Population)						(120,7,-34)	(129,4,-38)	(133,2,-40)	(138,1,-41)	(143,0,-43)
	Lupus (4)							(129,-56,22)	(134,-59,22)	(139,-61,23)	(145,-63,23)
	Taurus (C7 - L1527)							(-117,1,-25)	(-123,6,-28)	(-129,10,-30)	(-136,14,-33)
	Taurus (C8 - B213)							(-127,16,-44)	(-135,19,-44)	(-143,21,-43)	(-151,24,-43)
	Lupus (3)							(126,-48,24)	(132,-50,25)	(139,-52,25)	(146,-54,25)
	Taurus (D2 - L1558)							(-108,-12,-39)	(-113,-8,-41)	(-118,-4,-43)	(-123,0,-45)
	Lupus (Off-Cloud Population)							(128,-48,28)	(134,-49,29)	(140,-51,29)	(146,-52,29)
	Taurus (D1 - L1544)							(-143,-8,-18)	(-152,-6,-19)	(-161,-5,-20)	(-170,-3,-21)
	Taurus (C6 - L1524)								(-110,6,-29)	(-116,9,-32)	(-123,13,-34)
	Chamaeleon (1-South)								(86,-152,-43)	(84,-156,-47)	(82,-161,-51)
	Taurus (C5 - L1546)								(-141,8,-46)	(-148,10,-46)	(-155,12,-45)
	Taurus (D4 - North)								(-118,6,-34)	(-123,12,-36)	(-128,17,-38)
	Taurus (C1 - L1551)								(-126,1,-50)	(-131,1,-49)	(-136,2,-49)
	Chamaeleon (1-North)								(85,-157,-40)	(84,-161,-44)	(84,-165,-49)
	Chamaeleon (2)								(107,-151,-46)	(106,-154,-47)	(105,-158,-48)
	Taurus (C2 - L1495)									(-116,20,-32)	(-122,24,-35)
	Rho Oph "Young" (Population I)									(126,-16,42)	(131,-15,40)

The time sequence from left to right shows the (x,y,z) positions (in pc) of clusters as a function of time. If a cell appears blank, the cluster has not yet been born, with the first filled cell (from left to right) indicating the birth position of the cluster. These birth positions are used to fit the analytic superbubble expansion model presented in the Methods section. All positions are given with respect to the Local Standard of Rest. The rows are color-coded according to the cluster's longitude and map to the colors of the clouds shown in Figs. 1 and 2, as well as Extended Data Table 1. Significant events corresponding to each time step are summarized at top.